Atmos. Chem. Phys. Discuss., 15, 28317–28360, 2015
www.atmos-chem-phys-discuss.net/15/28317/2015/
doi:10.5194/acpd-15-28317-2015

Atmospheric Chemistry and Physics Discussions
Open Access
EGU

Mercury oxidation from bromine chemistry in the free troposphere over the southeastern US

S. Coburn[1,2], B. Dix[1], E. Edgerton[3], C. D. Holmes[4], D. Kinnison[5], Q. Liang[6], A. ter Schure[7], S. Wang[1,2,a], and R. Volkamer[1,2]

[1]Department of Chemistry and Biochemistry, University of Colorado Boulder, Boulder, CO, USA
[2]Cooperative Institute for Research in Environmental Sciences (CIRES), Boulder, CO, USA
[3]Atmospheric Research and Analysis (ARA) Inc., Plano, TX, USA
[4]Department of Earth, Ocean and Atmospheric Science, Florida State University, Tallahassee, FL, USA
[5]National Center for Atmospheric Research (NCAR), Boulder, CO, USA
[6]NASA Goddard Space Flight Center, Atmospheric Chemistry and Dynamics Branch, Greenbelt, MD 20771, USA
[7]Electric Power Research Institute (EPRI), Palo Alto, CA, USA
[a]now at: Department of Chemistry, University of Michigan, MI, USA

Received: 18 August 2015 – Accepted: 22 September 2015 – Published: 21 October 2015

Correspondence to: R. Volkamer (rainer.volkamer@colorado.edu)

Published by Copernicus Publications on behalf of the European Geosciences Union.

Abstract

The elevated deposition of atmospheric mercury over the Southeastern United States is currently not well understood. Here we measure partial columns and vertical profiles of bromine monoxide (BrO) radicals, a key component of mercury oxidation chemistry, to better understand the processes and altitudes at which mercury is being oxidized in the atmosphere. We use the data from a ground-based MAX-DOAS instrument located at a coastal site ~ 1 km from the Gulf of Mexico in Gulf Breeze, FL, where we had previously detected tropospheric BrO (Coburn et al., 2011). Our profile retrieval assimilates information about stratospheric BrO from the WACCM chemical transport model, and uses only measurements at moderately low solar zenith angles (SZA) to estimate the BrO slant column density contained in the reference spectrum (SCD_{Ref}). The approach has 2.6 degrees of freedom, and avoids spectroscopic complications that arise at high SZA; knowledge about SCD_{Ref} helps to maximize sensitivity in the free troposphere (FT). A cloud-free case study day with low aerosol load (9 April 2010) provided optimal conditions for distinguishing marine boundary layer (MBL: 0–1 km) and free tropospheric (FT: 1–15 km) BrO from the ground. The average daytime tropospheric BrO vertical column density (VCD) of $\sim 2.3 \times 10^{13}$ molec cm^{-2} (SZA < 70°) is consistent with our earlier reports on other days. The vertical profile locates essentially all tropospheric BrO above 4 km, and shows no evidence for BrO inside the MBL (detection limit < 0.5 pptv). BrO increases in the FT. The average FT-BrO mixing ratio was ~ 0.9 pptv between 1–15 km, consistent with recent aircraft observations. We find that the oxidation of gaseous elemental mercury (GEM) by bromine radicals to form gaseous oxidized mercury (GOM) is the dominant pathway for GEM oxidation throughout the troposphere above Gulf Breeze. The column integral oxidation rates range from 3.0–3.4 $\times 10^5$ molec cm^{-2} s^{-1} for bromine, while contributions from ozone (O_3) and chlorine (Cl) were 0.9×10^5 and 0.2×10^5 molec cm^{-2} s^{-1}, respectively. The GOM formation rate is sensitive to recently proposed atmospheric scavenging reactions of the HgBr adduct by nitrogen dioxide (NO_2), and to a lesser extent also HO_2 radicals. Using a

ACPD
15, 28317–28360, 2015

3-D chemical transport model, we find that surface GOM variations are typical also of other days, and are mainly derived from the free troposphere. Bromine chemistry is active in the FT over Gulf Breeze, where it forms water-soluble GOM that is subsequently available for wet scavenging by thunderstorms or transport to the boundary layer.

1 Introduction

Measurements of tropospheric halogen species are an area of increasing research interest due to the ability of halogens to destroy tropospheric ozone (O_3) (Read et al., 2008; Saiz-Lopez et al., 2012), oxidize atmospheric mercury (Holmes et al., 2009; Hynes et al., 2009), and modify oxidative capacity (Parella et al., 2012). Most assessments of the impacts of halogen chemistry are based on measurements of halogen oxides (bromine monoxide (BrO) and iodine monoxide (IO)), since these radicals are typically found at higher concentrations throughout the troposphere than the corresponding halogen atom radicals. Many of these studies take place in the planetary boundary layer (PBL) given that this region of the atmosphere is easily accessible from measurements located at the surface, and is also the most directly impacted by anthropogenic activities. However, halogen chemistry in the free troposphere (FT), albeit more challenging to measure, has the potential to affect an even larger air volume and mass. In particular, the colder temperatures of the free troposphere accelerate the bromine oxidation of gaseous elemental mercury (GEM) (Donohoue et al., 2006). Satellite-borne measurements represent a powerful resource for assessing global distributions and tropospheric vertical column densities (VCD) of BrO (GOME – van Roozendael et al., 2002; GOME-2 – Theys et al., 2011; Sihler et al., 2012). However, satellite retrievals rely on assumptions made about the vertical distribution of BrO, and uncertainties in these assumptions can lead to over/under predictions in the derived tropospheric VCD. The most direct method for measuring trace gas vertical distributions is through the use of aircraft (Prados-Ramon et al., 2011; Volkamer et al., 2015), or balloons (Fitzenberger et al., 2000; Dorf et al., 2006; Pundt et al., 2002). However, this type of measurement

ACPD
15, 28317–28360, 2015

is costly and potentially impractical if the goal is to establish long term trends in the FT. Ground-based measurements are typically more straightforward to deploy and maintain for extended periods of time, but optimizing ground-based capabilities to observe the FT remains an area of active research (Schofield et al., 2006; Theys et al., 2007; Hendrick et al., 2007; Coburn et al., 2011). Specifically, ground-based Multi-Axis Differential Optical Absorption Spectroscopy (MAX-DOAS) measurements are uniquely suited for this type of study since this technique also assesses vertical distributions, and derived VCDs can be directly compared with models and satellites. Additionally, the DOAS retrieval allows for the detection of not only BrO, but also other trace gases that have significant impacts on the chemical cycling of bromine species in the atmosphere, such as NO_2 and some volatile organic compounds (VOCs). However, measurements of FT BrO from ground-based MAX-DOAS are not straightforward for several reasons: (1) stratospheric BrO represents a large portion of the measured signal and creates a background that has to be accounted for when attempting to assess the FT, (2) ozone absorption structures are strongly present in the same wavelength region as BrO and can create interferences due to stratospheric ozone absorption, in particular at high solar zenith angles (SZA) (Aliwell et al., 2002; van Roozendael et al., 2002), and (3) the sensitivity of this technique peaks at the instrument altitude and decreases with increasing altitude. Recent advances with testing stratospheric BrO profiles in atmospheric models (Liang et al., 2014) provide opportunities to properly account for #1 by assimilating information from atmospheric models. Further, retrievals that avoid SZA larger 70° do not suffer from #2. Moreover, certain measurement geometries retain information about the FT. Figure S1 (Supplement) depicts the box Air Mass Factors (bAMFs), which represent the sensitivity of the slant column density (SCD) measurement geometry to BrO concentrations at different altitudes, for two pointing directions (or elevation angles, EA = 25 and 90° upwards) at several SZA; at SZA < 70° the sensitivity of these EAs peaks between 2–15 km. A more comprehensive view of the bAMFs for different EAs over a wider SZA range is shown in Fig. S2 (Supplement).

ACPD
15, 28317–28360, 2015

Van Roozendael et al. (2002) compared ground-based and balloon-borne measurements to VCDs of BrO from the space-borne Global Ozone Monitoring Experiment (GOME) and found all platforms were consistent with a rather widespread tropospheric BrO VCD of 1–3 $\times 10^{13}$ molec cm^{-2} once appropriate radiative transfer effects were taken into consideration. Salawitch et al. (2005) and Theys et al. (2011) also report satellite derived tropospheric BrO VCDs (GOME and GOME-2, respectively) for the mid-latitudes of 2 $\times 10^{13}$ and 1–3 $\times 10^{13}$ molec cm^{-2}, respectively. Ground based measurements (Theys et al., 2007; Coburn et al., 2011) in the mid-latitudes have reported BrO VCDs of 1–2 $\times 10^{13}$ molec cm^{-2} that are comparable to the findings from satellites. Volkamer et al. (2015) recently reported 1.6 $\times 10^{13}$ molec cm^{-2} BrO VCD in the tropics measured by limb-observations from aircraft. All of these studies point to the widespread presence of BrO in the FT, corresponding to a VCD of 1–3 $\times 10^{13}$ molec cm^{-2}. Based on these reports, tropospheric BrO could account for 20–30 % of a total BrO VCD ~ 5–6 $\times 10^{13}$ molec cm^{-2} as seen from satellite (van Roozendael et al., 2002; Theys et al., 2011), and significantly impact the lifetime of tropospheric O_3 and atmospheric GEM (Wang et al., 2015).

1.1 Atmospheric Hg in the southeastern US

Mercury in the atmosphere exists in three forms: gaseous elemental mercury (Hg^0, GEM), gaseous oxidized mercury in the form of either Hg^{2+} or Hg^{1+} (GOM), and particle-bound mercury (PBM). Understanding the processes that cycle mercury between its various forms (GEM $\leftrightarrow$ GOM $\leftrightarrow$ PBM) is of great importance because this speciation controls the deposition of mercury to the environment, i.e, GOM and PBM are more readily removed from the atmosphere via wet and dry deposition than GEM.(Lindberg and Stratton, 1998; Bullock, 2000). Once deposited, biological processes can methylate Hg^{2+} to form the neurotoxin methyl mercury, which bioaccumulates in fish. Enhancement factors for methyl mercury of up to 10^6 relative to water have been measured in predatory fish tissues (Schroeder and Munthe, 1998; Selin et al., 2010).

ACPD
15, 28317–28360, 2015

A better understanding of the processes controlling atmospheric mercury oxidation, and therewith removal, is particularly relevant for regions that experience high levels of mercury deposition, such as the southeastern United States (SE US). Figure 1 shows a map of the Total Mercury Wet Deposition in the US from 2013 (http://nadp.sws.uiuc.edu/maplib/pdf/mdn/hg_dep_2013.pdf). The high deposition levels experienced in the SE US cannot be explained by regional anthropogenic sources of mercury alone, which are mainly located within the Ohio River Valley where the prevailing winds carry emissions northeast. This indicates that a regional emission-deposition pattern is most likely not the major source–receptor relationship for mercury entering the environment over Florida, in the SE US, meaning that other possibilities, such as enhanced atmospheric oxidation followed by deposition, need to be explored.

2 Experimental

2.1 Atmospheric conditions

A case study during 9 April 2010 provided optimal conditions for assessing the ability of a ground-based MAX-DOAS instrument to measure FT trace gases (see Supplement for a brief overview of instrumentation and measurement site). Figure 2 shows a time series of trace gas differential slant column densities (dSCD) of BrO, IO, NO_2, and O_4 for the week surrounding the case study day; with 9 April highlighted by the blue box. The IO measurements are assimilated and used in the modeling portion of this study (Sect. 3.3), while the NO_2 measurements give an indication on the amount of influence from anthropogenic activities in the lowest layers of the BL. This day provides an excellent case study for two reasons: (1) consistent shape of the O_4 dSCDs across elevation angles as well as the clear splitting between the values is a good indicator for a cloud-free day, and (2) the relatively high O_4 dSCDs values (compared with other days) indicates a low aerosol load, enabling the instrument to realize longer light paths (increased sensitivity due to fewer extinction events), and an unobstructed view of the

ACPD
15, 28317–28360, 2015

FT. An inspection of webcam pictures for the instrument site proved the day to be free of visual clouds, and precursory look at the aerosol load confirmed the low values. Figure 2 also contains in-situ O_3 measurements (from both the US EPA site and a nearby Mercury Deposition Network (MDN) site) as well as wind direction measurements from a WeatherFlow, Inc. monitoring station located in Gulf Breeze, FL near the US EPA site.

Oxidized mercury measurements (Hg^{II} = GOM + PBM) at the Pensacola MDN site during study period (Edgerton et al., 2006) are also shown in the bottom panel of Fig. 2 (also Fig. 9, Sect. 3.3). On 9 April, Hg^{II} concentrations at the MDN site were rising from near zero on 8 April (due to rain) to peak values of 15–40 pg m^{-3} on the following days, which is above average for the season. In prior years, average daily peak concentrations at this site in spring were 15 pg m^{-3}, which is higher than during any other season (Weiss-Penzias et al., 2011; Nair et al., 2012). Observed GEM concentrations are persistently around 1.4 ng m^{-3} throughout early April, as expected for this season, and therefore not shown.

2.2 External model overview

The Whole Atmosphere Community Climate Model version 4 (WACCM4) (Garcia et al., 2007; Marsh et al., 2013) has been extensively evaluated for its representation of the stratosphere, including stratospheric BrO (SPARC CCMVal, 2010). The model does not represent tropospheric bromine sources from very short lived species (VSLS, bromocarbons); this is an active choice to assure a-priori information about tropospheric BrO represents a lower limit (see Sect. 2.4.1). However, $CHBr_3$ and CH_2Br_2 concentrations are fixed at the cold point and add about 5–6 pptv stratospheric Br_y (stratospheric Br_y loading is 21–22 pptv). In this work, WACCM is run with specified (external) meteorological fields. This is achieved by relaxing the horizontal winds and temperatures to reanalysis fields. The reanalysis fields used are taken from the NASA Global Modeling and Assimilation Office (GMAO) Modern-Era Retrospective Analysis for Research and Applications (MERRA) (Rienecker et al., 2011). The horizontal resolution is 1.9° × 2.5°

ACPD
15, 28317–28360, 2015

(latitude × longitude), with 88 vertical levels from the surface to the lower thermosphere (−140 km). Other WACCM model outputs used are: O_3, HCHO, NO_2, temperature, and pressure vertical profiles. Time synchronized BrO vertical profiles from WACCM are used as a-priori inputs to the inversion, while O_3, NO_2, and HCHO profiles are used as input for the box model utilized in this study (see Supplement). Temperature and pressure profiles were used to construct a molecular density profile in order to convert from concentration (output units of the inversion) to volume mixing ratios (VMR). Model data was generated specifically for this case study in order to best represent that atmospheric composition at the time of the measurements.

The GEOS-Chem global chemical transport model is used to provide a regional and seasonal context for the DOAS observations and their relevance to mercury chemistry. GEOS-Chem (v9-02, www.geos-chem.org) is driven by assimilated meteorology from the NASA Goddard Earth Observing System (GEOS-5). Simulations here have 2° × 2.5° horizontal resolution at 47 vertical layers for bromine and all species except mercury, which have 4° × 5° horizontal resolution. The bromine chemical mechanism, described by Parrella et al. (2012), includes marine bromocarbon emissions from Liang et al. (2010) and debromination of sea salt aerosols (Sander et al., 2003; Yang et al., 2005). Tropospheric bromine concentrations from GEOS-Chem are merged with stratospheric bromine from GEOS-CCM (Liang et al., 2010) to produce a complete atmospheric column. The mercury simulation is configured as described by Zhang et al. (2012), which includes GEM and two Hg^{II} species: GOM and PBM. Anthropogenic mercury emissions are from the US EPA National Emission Inventory (NEI) 2005 and National Pollutant Release Inventory (NPRI) 2005 inventories over North America (Zhang et al., 2012), which are adjusted to account for Hg^{II} reduction in power plant plumes (Landis et al., 2014), and elsewhere from the Global Emission Inventory Activity (GEIA) (Streets et al., 2009; Corbitt et al., 2011). Emissions and cycling from oceans and the biosphere are also included (Selin et al., 2008; Soerensen et al., 2010). Atmospheric GEM is oxidized by bromine (Holmes et al., 2010) using updated kinetic rate coefficients from Goodsite et al. (2012) and bromine concentrations from GEOS-

ACPD
15, 28317–28360, 2015

Chem. Hg^{II} partitions between GOM and PBM (Rutter et al., 2007; Amos et al., 2012) which are both quickly scavenged by precipitation or dry deposited, but also susceptible to reduction in cloud water. The bromine and mercury simulations are both spun up for at least one year. The model is then sampled hourly during April 2010 over Pensacola.

2.3 DOAS BrO retrieval

Following is a brief description of the parameters and settings used for the DOAS analysis of BrO for this study. A series of sensitivity studies on the BrO retrieval determined the optimal wavelength window for the analysis in this study to be 338–359 nm and include a 5th order polynomial. The reference cross sections used in the DOAS retrieval (WinDOAS software, Fayt and van Roozendael, 2001) were: O_3 (at 223 and 243 K, Bogumil et al., 2003), NO_2 (at 220 and 297 K, Vandaele et al., 1998), O_4 (at 293 K, Thalman and Volkamer, 2013), HCHO (Meller and Moortgat, 2000), BrO (Wilmouth et al., 1999), and a Ring spectrum (Chance and Spurr, 1997) calculated using the software DOASIS (Kraus, 2006) at 250 K for the reference used in the analysis. Additionally, a constant intensity offset was included in the fit, but limited to a range ($\pm 3 \times 10^{-3}$) determined by an estimation of the upper limit for the correction of spectrometer stray light. Details of the retrieval for other traces gases can be found in Table 1 along with an overview of the BrO retrieval settings listed here. A single zenith reference from a low SZA of the case study day was used to analyze all spectra (referred to as a fixed reference analysis); this spectrum was taken at ~ 13:01 UTC on 9 April 2010 (~ 23° SZA).

2.4 Inversion method

The retrieval of the BrO VCDs and vertical profiles for this study is a three-step process: (1) aerosol profiles are determined based on DOAS measurements of O_4 (see Supplement), (2) derived aerosol profiles are used in a Radiative Transfer Model (RTM) to calculate weighting functions for BrO (see Supplement for details on RTM calculation settings); and (3) weighing functions are used in an optimal estimation inversion

ACPD
15, 28317–28360, 2015

of the DOAS dSCDs to derive VCDs and vertical profiles (Sect. 2.4.1). Additionally, a method is presented here for determining the residual amount of BrO contained in the reference spectrum (SCD_{Ref}, Sect. 2.4.2). The relationship between SCD_{Ref} and the measured dSCDs is shown as Eq. (1).

$$SCD = dSCD + SCD_{Ref} \tag{1}$$

Both dSCDs and SCDs were used as input to the inversion, and sensitivity tests are presented to assess the impact of the SCD_{Ref} value on the derived vertical profiles and VCDs.

2.4.1 Trace gas inversion

Weighting functions calculated at 350 nm (for BrO) are used in an optimal estimation (OE) inversion (Rodgers, 2000) to determine the trace gas vertical profiles from the MAX-DOAS dSCD measurements, as given by Eq. (2).

$$x_r = x_a + A(x_t - x_a) \tag{2}$$

Here x_r represents the retrieved profile, x_a is the a-priori profile assumption, A is the averaging kernel matrix (AVK), and x_t is the true atmospheric state (represented by the MAX-DOAS dSCD or SCD measurements here). The AVK gives an indication of where the information in x_r is coming from, i.e. information from x_t (measurements) vs. x_a (a-priori assumption). The trace of this matrix gives the degrees of freedom (DoF) of the retrieval and indicates how many independent pieces of information are contained in the retrieval (see Sect. 3.1).

One important aspect in this study is the choice of the altitude grid used for both the radiative transfer calculations and the inversion. We used a grid of varying layer thickness: 0.5 km from 0–2 km; a single 3 km layer from 2–5 km, and 5 km layer thickness from 5–50 km. This grid is chosen to effectively combine the information from multiple altitudes into a single grid point to assure reasonable peaks in the averaging kernels at

ACPD
15, 28317–28360, 2015

increasing altitude, where the MAX-DOAS measurements have limited vertical resolution.

For the BrO inversion, four different a-priori profiles are used in order to assess the robustness of the inversion (see Fig. 5, Sect. 3.2, which shows three of the a-priori profiles along with their corresponding a-posteriori results). Two of the a-priori profiles are based on WACCM model output, the third used data from the CU Airborne-MAX-DOAS (AMAX-DOAS) instrument collected during the Tropical Ocean tRoposphere Exchange of Reactive halogen species and Oxygenated VOC (TORERO) 2012 field campaign (Volkamer et al., 2015), and the fourth is a mean profile from GEOS-CCM. The a-priori profiles from WACCM are: (1) direct model output for the time of each MAX-DOAS scan throughout the day (i.e., different a-priori profile for each MAX-DOAS scan), and (2) the profiles from (1) increased by 40 % (in VMR space). The a-priori profile for the TORERO case is derived from data collected during research flight 12 (RF12), which closely represents also the tropical average BrO profile (see Fig. 2 in Wang et al., 2015). The GEOS-CCM profile is a daytime zonal mean at 30° N. Both of these profiles are used to invert each scan. For reference, diurnal variations in the WACCM model output for BrO vertical distributions are shown in Fig. S3 (Supplement) panel (a), while panel (b) shows the corresponding tropospheric and total VCDs from these profiles. The a-priori profile error used as input to the OE is constructed based on upper limit values (in units of VMR) expected throughout the troposphere; this is set at 1 pptv for altitudes 0–2 km, 3 pptv for 2–5 km, and 4 pptv for 5–20 km (except for the GEOS-CCM case where this altitude range is set to 6 pptv to account for the extremely low values found in the a-priori). The a-priori error is constrained to 40 % for the stratospheric portion of the profile (20–50 km), based on the assumption that the WACCM profiles in this region of the atmosphere accurately represent the true atmospheric state, but allowing for sufficient room to reflect contributions of very short-lived organo halogen species (VSLS) to stratospheric BrO (Liang et al., 2014).

A similar method is also used to derive IO profiles (used as input to the modeling in Sect. 3.3). The IO inversion uses two a-priori profiles: (1) a moderate IO VMR in the

ACPD
15, 28317–28360, 2015

BL (0.2–0.5 pptv) and decreasing to very low levels (< 0.1 pptv) throughout the rest of the troposphere, and (2) profiles from recently reported AMAX-DOAS measurements (Dix et al., 2013; Volkamer et al., 2015). A summary of the a-priori profiles, example a-posteriori profiles, the average (for the case study) profile, and the diurnal variation in the VCD for IO is found is Fig. S4 (Supplement).

2.4.2 Determination of SCD_{Ref}

The BrO profile at the recording time of the fixed reference spectrum is included in the analysis by estimating the reference SCD (SCD_{Ref}) for BrO, which is then added to the dSCDs at off-axis EAs according to Eq. (1). Initial sensitivity studies revealed that some MAX-DOAS scans from the case study day are better suited for producing consistent values for SCD_{Ref} than others. The final choice of the reference spectrum is informed from comparing the SCD_{Ref} determined using the iterative method presented here to the SCD_{Ref} predicted by the WACCM a-priori profile (2) (see Sect. 2.4.1), which assumes a median BrO abundance. The ratio of SCD_{Ref} divided by the BrO VCD corresponds to the AMF of the reference spectrum, which in the case of our case study was ~ 1.2. The following criteria are applied to select a reference spectrum: (1) the SCD_{Ref} needs to be consistent with the AMF for the a-posteriori BrO profile, as well as (2) be within $\pm 1 \times 10^{13}$ molec cm^{-2} of the modified WACCM profile. Figure S5 (Supplement) shows the results from this approach for multiple zenith spectra (potential references) on the case study day, and thus illustrates the need for active measures, such as the above, to build internal consistency between the BrO SCD_{Ref}, BrO VCD, AMF, and forward RTM calculations of the a-priori and a-posteriori BrO profiles. The results presented in this paper are produced from a single reference spectrum (see Sect. 2.3); however, other references that pass the above quality assurance criteria would not alter our conclusions. Selecting another reference spectrum that meets the aforementioned criteria only increases the variability in the derived VCD by less than 9×10^{12} molec cm^{-2} (for any given single scan), and changing the a-priori assumption has also only a small effect on the VCDs ($\pm 1.5 \times 10^{12}$ molec cm^{-2} from average value).

ACPD
15, 28317–28360, 2015

Iterative Approach: the value of SCD_{Ref} is determined here by iteratively running the optimal estimation inversion on the MAX-DOAS scan containing the reference spectrum; this process is shown as flow chart in Fig. 3a. The initial value for SCD_{Ref} is determined from the a-priori profile, and subsequent SCD_{Ref} values are determined from the a-posteriori profile of the inversion returned from the previous iteration. For each iteration only SCD_{Ref} changes; the a-priori profile remains constant. After multiple iterations this method converges on a SCD_{Ref} that minimizes the differences between the measured and forward calculated scan SCD inputs. This value is then used as input for the inversion of the rest of the MAX-DOAS scans throughout the day. Figure 3b depicts the iterative refinement of the SCD_{Ref} and corresponding VCD for the reference chosen as most ideal for this case study.

3 Results and discussion

3.1 Characterizing the BrO profile retrieval

Figure 4 compares the AVK resulting from the OE inversion of BrO SCDs constructed by accounting for SCD_{Ref} (addition of this value to the measured dSCD output from the DOAS analysis prior to inversion) vs. not accounting for SCD_{Ref} (where SCD = dSCD and with appropriate modification of the weighting functions to reflect this treatment). The largest differences are seen at low SZA in the FT. Panel (a) shows the AVK matrix, which gives an indication as to how much information can be derived from the measurements at specific altitudes, as a function of altitude for the inversion (at SZA = 25°) accounting for SCD_{Ref} (different colored thin lines) along with the diagonal of this matrix (thick black line) and the diagonal for the inversion not accounting for SCD_{Ref} (thick red line). Figure 4b shows the difference between the two diagonals as a function of altitude. Also listed in Fig. 4 are DoFs for the different retrieval methods, which demonstrate an increase of 0.5 (mostly coming from the FT) when SCD_{Ref} is properly accounted for. For these reasons, we chose to include SCD_{Ref} in the inversion of the

ACPD
15, 28317–28360, 2015

measured BrO dSCDs in order to further maximize the sensitivity of these measurements towards the FT. Additional information on the DoFs and inversion RMS for these retrievals throughout the case study day are found in Fig. S6 (Supplement).

Recently, Volkamer et al. (2015) reported significant sensitivity of MAX-DOAS profiles to the magnitude of SCD_{Ref} over oceans, for case studies where independent aircraft measurements show that a significant trace gas partial column resides above the BL (IO and glyoxal). They find that while the BL VMR is insensitive to the value of SCD_{Ref}, the partial tropospheric VCD can be impacted by up to a factor of 2–3. During this study the impact of using BrO dSCDs, rather than SCDs, in the inversion lead to an average percent difference in the BrO VCD derived for each MAX-DOAS scan of $\sim 30\,\%$. The average VCDs were 2.1×10^{13} and 2.3×10^{13} molec cm^{-2} (integrated from 0–15 km) when using dSCDs or SCDs (only $\sim 10\,\%$ difference). This reflects that the inversion based on dSCDs (not accounting for SCD_{Ref}) produced highly variable FT VCDs throughout the case study day, and that this variability is reduced for the SCD based inversion.

The reduced variability in the BrO VCD compared to the other gases investigated by Volkamer et al. (2015) is probably due to the fact that no BrO was detected in the BL in either case study. For glyoxal and IO about 50 % of the VCD resides near the instrument altitude (Volkamer et al., 2015). This BL contribution adds offsets to the SCDs also for the higher EAs that "partially obstruct" the view of the FT, and makes FT partial columns subject to larger error bars. The lack of BrO in the BL seems to simplify measurements of FT partial columns from the ground. The Volkamer et al. case studies in combination with our results thus suggest that MAX-DOAS instruments that are to measure FT partial columns of gases other than BrO should actively avoid complications from absorbers near instrument altitude, for example by placing the instrument on mountaintops. The lack of aerosols from high mountaintops has the additional benefit of increased sensitivity to measure profiles for BrO and other gases.

ACPD
15, 28317–28360, 2015

3.2 BrO VCDs and vertical profiles

Figure 5 shows the results from the inversions using the three different a-priori profiles. Panel (a) shows the a-priori profiles, and the a-posteriori vertical profiles corresponding to one scan at ~ 23° SZA (around solar noon), as well as the median profile from all profiles. A total of 45 profiles, corresponding to SZA < 70° for each a-priori case, were combined to create the median BrO vertical profile for the case study day (Fig. 5). The median profile was used for the modeling results and discussion in Sect. 3.3. Panel (b) shows the AVK (see Sect. 2.4.1) from the inversion using the un-modified WACCM BrO output as the a-priori profile. In an ideal scenario, the AVK for each layer peaks near unity within that layer. The derived vertical profiles show only slight dependence on the a-priori profile with a maximum average difference between a-posteriori profiles of ~ 0.6 ppt at altitudes < 15 km for the entire day. These profile differences have only a small effect on the free tropospheric VCDs, i.e. < 20 % difference for SZA < 70°. The AVK peaks twice – once in the lowest layer (from the lowest looking elevation angles) and again between 5 and 20 km, which reflects the combination of the optimization of the radiative transfer grid and the measurement sensitivity. This is interpreted as an indication that the DoFs remaining after accounting for the peak at instrument altitude correspond to the FT. Figure S7 (Supplement) contains a comparison of the a-posteriori profile derived BrO dSCDs and the measured dSCDs (panels a and b) and the corresponding RMS difference between measured and calculated dSCDs in panel (c).

This inversion procedure allows for the determination of the diurnal variation in the BL (0–1 km), FT (1–15 km), and total VCDs for BrO. These results, corresponding to the inversion utilizing WACCM output as the a-priori profile, are found in Fig. 6b along with the corresponding DoF panel (a). The errors bars on the tropospheric and stratospheric VCDs reflect the range of derived values resulting from the use of different a-priori assumptions. The retrieved diurnal variation in the free tropospheric (1–15 km) BrO VCD follows that of the total VCD with an average of 53 % contribution to the total and varying

ACPD
15, 28317–28360, 2015

between 47–57 % throughout the day; this corresponds to a daytime average VCD of $\sim 2.3 \pm 0.16 \times 10^{13}$ molec cm^{-2}, where the error reflects the average error on the VCD as seen in Fig. 6b. The overall error on the average VCD is $\sim 0.7 \times 10^{13}$ molec cm^{-2} and takes into account change in the VCD when assuming the maximum profile error given by the OE inversion. This treatment is expressed in Eq. (3).

$$\text{Total Error} = \frac{(\text{VCD}_{\text{Prf}} - \text{VCD}_{\text{Prf+OE err}})}{2} \tag{3}$$

where VCD_{Prf} is the VCD calculated directly from the OE inversion a-posteriori, $\text{VCD}_{\text{Prf+OE err}}$ is the VCD calculated from the OE inversion a-posteriori profile plus the OE error of that profile, and the factor of 2 reflects that the OE inversion error at each altitude covers oscillations both higher and lower than the retrieved profile at that point.

The derived tropospheric VCD from this study falls directly in the range of other currently reported measurements, which span from ~ 1–3×10^{13} molec cm^{-2}. This value is higher than other ground based measurements (in the Southern Hemisphere Tropics) (Theys et al., 2007), which reported tropospheric VCDs of 1.1–1.2×10^{13} molec cm^{-2}, but still well within the overall range of other studies. Global model results for BrO VCDs predict much lower columns than observed in this study. Yang et al. (2005), using the p-TOMCAT model, found mid-latitudes values of $\sim 0.4 \times 10^{13}$ molec cm^{-2} for spring/summer months; and Parrella et al. (2012), using GEOS-Chem, reported values of $< 1 \times 10^{13}$ molec cm^{-2} for the entire year for the Northern Hemisphere mid-latitudes. The value from Parella et al. (2012) is slightly more comparable to that predicted by WACCM for the case study day ($\sim 1 \times 10^{13}$ molec cm^{-2}, see Fig. S3, Supplement).

3.3 Modeling

Mercury oxidation rates: the primary finding from a comparison of the Hg^0 oxidation rates for the three radical species tested in this study (Br, O_3, and Cl) is that the reaction with Br dominates the overall rate throughout the troposphere, independent of initial BrO vertical profile used. The column integral rates are 9.3×10^4 and

ACPD
15, 28317–28360, 2015

1.7×10^4 molec cm^{-2} s^{-1} for O_3 and Cl, respectively; while the Br rates are 3.0×10^5 and 3.4×10^5 for the BrO vertical profiles from the MAX-DOAS measurements and GEOS-Chem respectively. The reaction rates from Br are at least a factor of 3 greater than the contribution from O_3. Cl is deemed to be negligible at the estimated concentrations used in this study. The vertically resolved rates are shown in Fig. 7a for all three reactions: Br (solid blue and dotted pink traces representing the BrO profiles from the MAX-DOAS measurements and GEOS-Chem, respectively, used to derive the Br radical concentrations); O_3 (red trace); and Cl (green trace); reflecting the contributions of these reactions at different altitudes. Also included in Fig. 7b are the corresponding lifetimes of GEM (as a function of altitude) against oxidation by the three molecules. Only in the lowest layers of the atmosphere do the rates of oxidation through reaction with O_3 become comparable or greater than those of the reaction with Br. However, it should be noted that for the cases where the rate of reaction with O_3 dominates, the BrO VMR in the lower layers is < 0.03 pptv while the O_3 VMR is ~ 50 ppbv, and in cases where reaction with Br dominates (at altitudes below 4 km) the BrO VMR is still < 0.3 pptv. The BrO vertical profile from the MAX-DOAS instrument below 4 km contains the highest amount of uncertainty because BrO is essentially zero within the variability of the measurements. The column integral rates of oxidation based on the MAX-DOAS measurements and the BrO profile from GEOS-Chem are actually quite similar (only ~ 6 % difference), which is most likely due to the additional bromine chemistry included in this model (see Sect. 2.2); however, the discrepancies in the vertical distribution of BrO lead to a mismatch in the altitudes at which the oxidation can occur. For both BrO profiles, the reaction with Br dominates above 4 km (indicated by the black dashed line in Fig. 7). Altitudes above 4 km are responsible for ~ 72 % of the column integral rate of GEM oxidation (through reaction with Br) based on the MAX-DOAS measurements; while that value decreases to ~ 55 % for the bromine profile from GEOS-Chem.

Mercury oxidation pathways: Fig. 8 shows the results of the "traditional" (panel a) and "revised" (panel b) HgBr scavenging schemes (see Supplement for descriptions) on the rate of GEM oxidation as a function of altitude. In each panel, contributions of

ACPD
15, 28317–28360, 2015

individual molecules (colored lines) are shown along with the total removal rate (black lines). Panel (c) shows the vertical profile of the ratio of the "revised" total rate to "traditional" total rate, which demonstrates the enhanced oxidation of HgBr when considering the additional scavenging reactions. In the "traditional" model the percent contributions to the column integrated rate of oxidation of HgBr are 71.3 and 28.7 % for OH and Br, respectively; and in the "revised" model the percent contributions are as follows: 86.1 % (NO_2); 10.6 % (HO_2); 1.8 % (BrO); 0.9 % (OH); 0.3 % (Br); 0.2 % (IO); and < 0.1 % (I). Note that mercury oxidation is initiated by reaction between Br radicals and GEM in both reaction schemes, and the additional scavenging reactions in the "revised" scheme primarily increase the overall rate of oxidation at altitudes where HgBr decomposition is fast. The greatest enhancement is seen below 8 km, where the overall rate of oxidation is ~ 20 times faster, primarily because of the reaction of HgBr with NO_2 and HO_2.

Figure 8 also illustrates the increased number of species produced from the additional oxidation mechanisms, some of which may have physical and chemical properties that differ from the two products of the "traditional" mode, which are also products in the "revised" scenario but are present at much lower concentrations. In the "traditional" scenario at 1 km, the scavenging products HgBrOH and $HgBr_2$ account for 96 and 4 % of the total HgBrX, respectively, and these values drop to 0.2 % and ≪ 0.1 % in the "revised" scenario where $HgBrNO_2$ accounts for 95 % of HgBrX. In the "revised" scenario, $HgBrNO_2$ remains the major product throughout the atmosphere, but at free tropospheric altitudes $HgBrHO_2$ also contributes significantly at 35 %, compared to $HgBrNO_2$ at 59 %. There are currently no observations of the molecular composition of GOM with which to evaluate these simulated product distributions.

Mercury lifetime with respect to oxidation: the above oxidation rates correspond to a minimum lifetime of GEM with respect to oxidation by bromine radicals of ~ 40 days in the FT (based on the MAX-DOAS measurements). The total tropospheric column average lifetimes are 62, 88, and 63 days for the scenarios including BrO profiles from the MAX-DOAS measurements, WACCM, and GEOS-Chem, respectively, where in

ACPD
15, 28317–28360, 2015

each case the contribution from the reactions with O_3 and Cl are the same and the differences are owing to the differing amounts of Br radicals. This is much shorter than the currently expected atmospheric lifetime on the order of several months. However, the box model only accounts for partitioning of the GOM species between the gas phase and aerosols; once they are in the aqueous phase they can be photo-reduced to GEM that can then subsequently return to the gas phase (Costa and Liss, 1999), thus extending the effective lifetime significantly beyond that calculated above. The kinetic coefficients for reactions involving HgBr come mainly from quantum chemical calculations, which have significant uncertainties, so the simulated GEM lifetime could be extended by reducing the rate coefficients within their uncertainties. Another possible mechanism is the photo-dissociation of HgBrX products containing species that have significant absorption cross-sections in the ultra-violet/visible (UV/Vis) region of the electromagnetic radiation spectrum, e.g. $HgBrNO_2$, $HgBrHO_2$, which could reproduce HgBr. This HgBr could then thermally decompose to re-form GEM, or be oxidized again. Our observations are consistent with previous findings (Wang et al., 2015), that establish GEM as a chemically highly dynamic component of the FT. It is expected that GOM species will go through additional processes also in the aqueous phase, which could significantly impact the ultimate fate of the mercury.

Atmospheric implications: the rapid oxidation of mercury in the lower FT is of potential relevance in the SE US, where there have been several studies linking deep convective activity to the elevated levels of mercury found in rainwater (Guentzel et al., 2001; Landing et al., 2010; Nair et al., 2013). The bio-accumulation of methyl mercury in fish tissues is particularly relevant in this region, where it has been deemed unsafe to eat fish harvested from many lakes in the region (Engle et al., 2008; Liu et al., 2008). Wet deposition measurements of mercury exceed what can be explained through regional sources in the southeast. In fact, Guentzel et al. (2001) estimated that < 46 % of the mercury deposited in Florida was a result of local emissions, the other > 50 % was attributed to long-range transport of mercury in the atmosphere; the transported fraction may have increased since those data were collected in the 1990s because regional

ACPD
15, 28317–28360, 2015

US mercury emissions have declined while global emissions have risen. This attribution, coupled with mountaintop and aircraft studies locating elevated levels of GOM in the free troposphere (Swartzendruber et al., 2006; Faïn et al., 2009; Swartzendruber et al., 2009; Lyman and Jaffe, 2012; Brooks et al., 2014; Weiss-Penzias et al., 2015), strongly suggests the presence of a global "pool" of mercury in the upper atmosphere that contributes to widespread mercury deposition on a local to regional scale.

On the case study day, Hg^{II} (= GOM + PBM) concentrations at the nearly Pensacola MDN site reached 25 pg m^{-3} around midday and nearly 40 pg m^{-3} on 10 April (Fig. 9). High Hg^{II} events in Pensacola are frequently consistent with emissions from a nearby coal-fired power plant, however about 25 % of such events have significant contributions from the free troposphere (Weiss-Penzias et al., 2011). The high $Hg^{II}:SO_2$ ratios (10–20 pg m^{-3} ppb^{-1}) and high $NO_y:SO_2$ ratios (3.5–5.2 ppb ppb^{-1}) recorded on 9–10 April make the power plant an unlikely source of the Hg^{II} on these days (Fig. S8); for comparison, Weiss-Penzias et al. (2011) reported $Hg^{II}:SO_2$ and $NO_y:SO_2$ ratios of 3.5 and 1.0, respectively, in power plant plumes. Like Hg^{II} concentrations, ozone concentrations and Hg^{II} dry deposition in Florida also peak in spring, all of which are consistent with a significant source of surface Hg^{II} being from the upper troposphere (Lyman et al., 2009; Sexaur Gustin et al., 2012). We use the GEOS-Chem model to further probe the sources of this Hg^{II}. Figure 9 shows that the model generally reproduces the day-to-day variability of Hg^{II} observations during April 2010 (but not extremes), such as the low concentrations during 7–8 April and relative maxima on 5 and 10 April. In both the model and observations, Hg^{II} concentrations rise abruptly in the morning, consistent with entrainment of Hg^{II} aloft, and unlike the other combustion tracers (e.g. NO_y, SO_2) that reach high concentrations at night (Fig. S8 in the Supplement). The model does not reproduce the abrupt drop in Hg^{II} around 18:00 CST, however, which may be partly due to local sea breeze circulations that are evident in wind observations but not simulated at the 4° × 5° model resolution. In addition, mixing depth errors in the driving meteorology are known to affect other species, particularly at night (Lin et al.,

ACPD
15, 28317–28360, 2015

2010; McGrath-Spangler and Molod, 2014). To assess the contribution of the free troposphere to surface Hg^{II} during April 2010, we conduct an additional model simulation with zero anthropogenic emissions in North America and no mercury redox chemistry in the lower troposphere (> 700 hPa). The simulation is initialized from the base run on 1 April. Due to its fast deposition, all boundary-layer Hg^{II} in the sensitivity simulation after about 1 day originates from oxidation of GEM in the free troposphere or, less likely, from intercontinental transport of anthropogenic Hg^{II}. Figure 9 shows there is little difference between the base and sensitivity simulations, meaning that the FT is the main source of boundary-layer Hg^{II} in the model and that variability in the FT component explains most of the day-to-day Hg^{II} variability. Thus, the 3-D model shows that conditions on 9 April are favorable for Hg^{II} transport to the boundary layer, exactly when the DOAS observations find substantial amounts of BrO are present in the free troposphere.

The GEM oxidation mechanism in the 3-D model corresponds to the "traditional" scheme in the box model and bromine concentrations in GEOS-Chem are lower than recent aircraft observations (Volkamer et al., 2015), so the GEM oxidation may be faster than simulated. Greater Hg^{II} production in the free troposphere might help correct the model's 20 % low bias in mercury wet deposition over the Southeast US (Zhang et al., 2012), but this would depend on the rate of any compensating reduction reaction, as discussed above. The findings of this study indicate that the amount of bromine located in the FT is sufficient to quickly oxidize GEM.

4 Conclusions

We show the benefits of determining SCD_{Ref} to maximize the sensitivity of ground based MAX-DOAS measurements to detect BrO in the FT, and improve the overall consistency of time-resolved BrO tropospheric VCDs. The retrieval can also be applied to other trace gases. Knowledge of SCD_{Ref} allows retrievals at higher altitudes,

ACPD
15, 28317–28360, 2015

i.e., the derivation of one vertical profile for each MAX-DOAS scan throughout the day (SZA < 70°) and the assessment of the diurnal variation of the partial BrO vertical columns. Our retrieval is complementary to previous studies that have characterized the stratosphere using zenith-sky measurements under twilight conditions (Theys et al., 2007; Hendrick et al., 2007), and minimizes the influence of O_3 absorption, and the contribution of stratospheric BrO to the overall BrO signal by using CTM output to constrain stratospheric BrO in combination with BrO dSCDs measured at low SZA instead. The FT VCDs reported here are in good agreement with the previously cited values for BrO, with the average BrO FT VCD ($\sim 2.3 \times 10^{13}$ molec cm^{-2}) falling within the range reported by other studies ($1–3 \times 10^{13}$ molec cm^{-2}) (see Wang et al., 2015, and references therein). These measurements all point to the presence of background amounts of BrO in the FT that is larger than current models predict.

The presented box model studies indicate that bromine radicals are the dominant oxidant for atmospheric GEM throughout the FT above the studied region. Our results confirm that mercury is rapidly oxidized by bromine, and a chemically highly dynamic species in the atmosphere. The chemical lifetime of GEM is ~ 40 days in the tropical FT based on calculations presented in this study; longer GEM global lifetimes should thus be regarded to indicate "effective lifetimes", i.e., are the result of rapid chemical cycling of GOM back to GEM. Mercury measurements during our study period show high surface Hg^{II} concentrations that likely originate in the FT, meaning that we have observed substantial BrO columns under conditions favorable for Hg^{II} transport to the boundary layer. Additionally, this study suggests that the experimental observation of elevated GOM in the FT may be linked to our incomplete understanding about tropospheric bromine sources (Swartzendruber et al., 2006; Faïn et al., 2009; Lyman and Jaffe, 2012; Wang et al., 2015; Shah et al., 2015). The findings of this study indicate that the amount of bromine located in the FT above the (coastal regions) of the SE US is sufficient to quickly oxidize GEM to GOM, which in turn can be wet deposited, and as such can help explain the observed elevated wet deposition pattern in this region. Our results highlight the need to understand BrO vertical profiles in the FT, and represent

ACPD
15, 28317–28360, 2015

them in atmospheric models to understand the location where mercury is oxidized in the atmosphere, and available for wet and dry deposition. More studies are needed to test and represent the bromine sources in atmospheric models, test atmospheric GOM abundances by field data, clarify the chemical identity of GOM, its global distributions, and dry and wet removal.

The Supplement related to this article is available online at doi:10.5194/acpd-15-28317-2015-supplement.

Acknowledgements. S. Coburn is the recipient of a NASA Earth and Space Science graduate fellowship. The CU MAX-DOAS instrument was developed with support from the EPRI's Technology Innovation program (EP-P27450/C13049). Additional support from EPRI (EP-P32238/C14974), and US National Science Foundation (ATM-0847793, AGS-1104104), and CU Boulder startup funds is gratefully acknowledged.

References

Aliwell, S. R., van Roozendael, M., Johnston, P. V., Richter, A., Wagner, T., Arlander, D. W., Burrows, J. P., Fish, D. J., Jones, R. L., Tørnkvist, K. K., Lambert, J.-C., Pfeilsticker, K., and Pundt, I.: Analysis of BrO in zenith-sky spectra: an intercomparison exercise for analysis improvement, ACH 10-1–ACH 10-20, J. Geophys. Res.-Atmos., 107, D14, doi:10.1029/2001JD000329, 2002.

Amos, H. M., Jacob, D. J., Holmes, C. D., Fisher, J. A., Wang, Q., Yantosca, R. M., Corbitt, E. S., Galarneau, E., Rutter, A. P., Gustin, M. S., Steffen, A., Schauer, J. J., Graydon, J. A., Louis, V. L. St., Talbot, R. W., Edgerton, E. S., Zhang, Y., and Sunderland, E. M.: Gas-particle partitioning of atmospheric Hg(II) and its effect on global mercury deposition, Atmos. Chem. Phys., 12, 591–603, doi:10.5194/acp-12-591-2012, 2012.

Balabanov, N., Shepler, B., and Peterson, K.: Accurate global potential energy surface and reaction dynamics for the ground state of $HgBr_2$, J. Phys. Chem. A, 109, 8765–8773, doi:10.1021/jp0534151, 2005.

ACPD
15, 28317–28360, 2015

Bogumil, K., Orphal, J., Homann, T., Voigt, S., Spietz, P., Fleischmann, O., Vogel, A., Hartmann, M., Kromminga, H., Bovensmann, H., Frerick, J., and Burrows, J.: Measurements of molecular absorption spectra with the SCIAMACHY pre-flight model: instrument characterization and reference data for atmospheric remote-sensing in the 230–2380 nm region, J. Photoch. Photobio. A, 157, 167–184, doi:10.1016/S1010-6030(03)00062-5, 2003.

Brooks, S., Ren, X., Cohen, M., Luke, W. T., Kelley, P., Artz, R., Hynes, A., Landing, W., and Martos, B.: Airborne vertical profiling of mercury speciation near Tullahoma, TN, USA, Atmosphere, 5, 557–574, doi:10.3390/atmos5030557, 2014.

Bullock, O.: Modeling assessment of transport and deposition patterns of anthropogenic mercury air emissions in the United States and Canada, Sci. Total Environ., 259, 145–157, 2000.

Chance, K. and Spurr, R.: Ring effect studies: Rayleigh scattering, including molecular parameters for rotational Raman scattering, and the Fraunhofer spectrum, Appl. Optics, 36, 5224–5230, doi:10.1364/AO.36.005224, 1997.

Coburn, S., Dix, B., Sinreich, R., and Volkamer, R.: The CU ground MAX-DOAS instrument: characterization of RMS noise limitations and first measurements near Pensacola, FL of BrO, IO, and CHOCHO, Atmos. Meas. Tech., 4, 2421–2439, doi:10.5194/amt-4-2421-2011, 2011.

Corbitt, E. S., Jacob, D. J., Holmes, C. D., Streets, D. G., and Sunderland, E. M.: Global source–receptor relationships for mercury deposition under present-day and 2050 emissions scenarios, Environ. Sci. Technol., 45, 10477–10484, doi:10.1021/es202496y, 2011.

Costa, M. and Liss, P. S.: Photoreduction of mercury in seawater and its possible implications for Hg^0 air–sea fluxes, Mar. Chem., 68, 87–95, doi:10.1016/S0304-4203(99)00067-5, 1999.

Crawford, J., Davis, D., Olson, J., Chen, G., Liu, S., Gregory, G., Barrick, J., Sachse, G., Sandholm, S., Heikes, B., Singh, H., and Blake, D.: Assessment of upper tropospheric HO_x sources over the tropical Pacific based on NASA GTE/PEM data: net effect on HOx and other photochemical parameters, J. Geophys. Res.-Atmos., 104, 16255–16273, doi:10.1029/1999JD900106, 1999.

Deutschmann, T., Beirle, S., Friess, U., Grzegorski, M., Kern, C., Kritten, L., Platt, U., Prados-Roman, C., Pukite, J., Wagner, T., Werner, B., and Pfeilsticker, K.: The Monte Carlo atmospheric radiative transfer model McArtim: introduction and validation of Jacobians and 3D features, J. Quant. Spectrosc. Ra., 112, 1119–1137, doi:10.1016/j.jqsrt.2010.12.009, 2011.

ACPD
15, 28317–28360, 2015

Mercury oxidation from bromine chemistry in the free troposphere over the southeastern US

S. Coburn et al.

Dibble, T. S., Zelie, M. J., and Mao, H.: Thermodynamics of reactions of ClHg and BrHg radicals with atmospherically abundant free radicals, Atmos. Chem. Phys., 12, 10271–10279, doi:10.5194/acp-12-10271-2012, 2012.

Dix, B., Baidar, S., Bresch, J. F., Hall, S. R., Schmidt, K. S., Wang, S., and Volkamer, R.: Detection of iodine monoxide in the tropical free troposphere, P. Natl. Acad. Sci. USA, 110, 2035–2040, doi:10.1073/pnas.1212386110, 2013.

Donohoue, D., Bauer, D., and Hynes, A.: Temperature and pressure dependent rate coefficients for the reaction of Hg with Cl and the reaction of Cl with Cl: a pulsed laser photolysis-pulsed laser induced fluorescence study, J. Phys. Chem. A, 109, 7732–7741, doi:10.1021/jp0513541, 2005.

Donohoue, D., Bauer, D., Cossairt, B., and Hynes, A.: Temperature and pressure dependent rate coefficients for the reaction of Hg with Br and the reaction of Br with Br: a pulsed laser photolysis-pulsed laser induced fluorescence study, J. Phys. Chem. A, 110, 6623–6632, doi:10.1021/jp054688j, 2006.

Dorf, M., Bösch, H., Butz, A., Camy-Peyret, C., Chipperfield, M. P., Engel, A., Goutail, F., Grunow, K., Hendrick, F., Hrechanyy, S., Naujokat, B., Pommereau, J.-P., Van Roozendael, M., Sioris, C., Stroh, F., Weidner, F., and Pfeilsticker, K.: Balloon-borne stratospheric BrO measurements: comparison with Envisat/SCIAMACHY BrO limb profiles, Atmos. Chem. Phys., 6, 2483–2501, doi:10.5194/acp-6-2483-2006, 2006.

Edgerton, E. S., Hartsell, B. E., and Jansen, J. J.: Mercury speciation in coal-fired power plant plumes observed at three surface sites in the southeastern US, Environ. Sci. Technol., 40, 4563–4570, doi:10.1021/es0515607, 2006.

Engle, M. A., Tate, M. T., Krabbenhoft, D. P., Kolker, A., Olson, M. L., Edgerton, E. S., DeWild, J. F., and McPherson, A. K.: Characterization and cycling of atmospheric mercury along the central US Gulf Coast, Appl. Geochem., 23, 419–437, doi:10.1016/j.apgeochem2007.12.024, 2008.

Eyring, V., Shepherd, T. G., and Waugh, D. W. (Eds.): SPARC CCMVal, SPARC Report on the Evaluation of Chemistry-Climate Models, SPARC Report No. 5, WCRP-132, WMO/TD-No. 1526, available at: http://www.atmosp.physics.utoronto.ca/SPARC/ccmval_final/coverpage.pdf (last access: 19 October 2015), 2010.

Faïn, X., Obrist, D., Hallar, A. G., Mccubbin, I., and Rahn, T.: High levels of reactive gaseous mercury observed at a high elevation research laboratory in the Rocky Mountains, Atmos. Chem. Phys., 9, 8049–8060, doi:10.5194/acp-9-8049-2009, 2009.

ACPD
15, 28317–28360, 2015

Fayt, C. and van Roozendael, M.: WinDoas 2.1 – Software User Manual, 2001.
Fitzenberger, R., Bösch, H., Camy-Peyret, C., Chipperfield, M. P., Harder, H., Platt, U., Sinnhuber, B.-M., Wagner, T., and Pfeilsticker, K.: First profile measurements of tropospheric BrO, 2921–2924, Geophys. Res. Lett., 27, 18, doi:10.1029/2000GL011531, 2000.
Garcia, R. R., Marsh, D. R., Kinnison, D. E., Boville, B. A., and Sassi, F.: Simulation of secular trends in the middle atmosphere, 1950–2003, J. Geophys. Res.-Atmos., 112, D09301, doi:10.1029/2006JD007485, 2007.
Goodsite, M. E., Plane, J. M. C., and Skov, H.: A theoretical study of the oxidation of Hg^0 to $HgBr_2$ in the troposphere, Environ. Sci. Technol., 38, 1772–1776, doi:10.1021/es034680s, 2004.
Goodsite, M. E., Plane, J. M. C., and Skov, H.: Correction to a theoretical study of the oxidation of Hg^0 to $HgBr_2$ in the Troposphere, Environ. Sci. Technol., 46, 5262–5262, doi:10.1021/es301201c, 2012.
Guentzel, J., Landing, W., Gill, G., and Pollman, C.: Processes influencing rainfall deposition of mercury in Florida, Environ. Sci. Technol., 35, 863–873, doi:10.1021/es.001523+, 2001.
Hall, B.: The gas-phase oxidation of elemental mercury by ozone, Water Air Soil Poll., 80, 301–315, doi:10.1007/BF01189680, 1995.
Hendrick, F., Van Roozendael, M., Chipperfield, M. P., Dorf, M., Goutail, F., Yang, X., Fayt, C., Hermans, C., Pfeilsticker, K., Pommereau, J.-P., Pyle, J. A., Theys, N., and De Mazière, M.: Retrieval of stratospheric and tropospheric BrO profiles and columns using ground-based zenith-sky DOAS observations at Harestua, 60° N, Atmos. Chem. Phys., 7, 4869–4885, doi:10.5194/acp-7-4869-2007, 2007.
Holmes, C. D., Jacob, D. J., Mason, R. P., and Jaffe, D. A.: Sources and deposition of reactive gaseous mercury in the marine atmosphere, Atmos. Environ., 43, 2278–2285, doi:10.1016/j.atmosenv.2009.01.051, 2009.
Holmes, C. D., Jacob, D. J., Corbitt, E. S., Mao, J., Yang, X., Talbot, R., and Slemr, F.: Global atmospheric model for mercury including oxidation by bromine atoms, Atmos. Chem. Phys., 10, 12037–12057, doi:10.5194/acp-10-12037-2010, 2010.
Hynes, A., Donohoue, D., Goodsite, M., and Hedgecock, I.: Our current understanding of major chemical and physical processes affecting mercury dynamics in the atmosphere and at the air-water/terrestrial interfaces, in: Mercury Fate and Transport in the Global Atmosphere, edited by: Mason, R. and Pirrone, N., Springer, New York, NY, USA, 427–457, doi:10.1007/978-0-387-93958-2, 2009.

ACPD
15, 28317–28360, 2015

Kraus, S.: DOASIS – A Framework Design for DOAS, Shaker Verlag, University of Heidelberg, Germany, 2006.

Landing, W. M., Caffrey, J. M., Nolek, S. D., Gosnell, K. J., and Parker, W. C.: Atmospheric wet deposition of mercury and other trace elements in Pensacola, Florida, Atmos. Chem. Phys., 10, 4867–4877, doi:10.5194/acp-10-4867-2010, 2010.

Landis, M. S., Ryan, J. V., ter Schure, A. F. H., and Laudal, D.: Behavior of mercury emissions from a commercial coal-fired power plant: the relationship between stack speciation and near-field plume measurements, Environ. Sci. Technol., 48, 13540–13548, doi:10.1021/es500783t, 2014.

Liang, Q., Stolarski, R. S., Kawa, S. R., Nielsen, J. E., Douglass, A. R., Rodriguez, J. M., Blake, D. R., Atlas, E. L., and Ott, L. E.: Finding the missing stratospheric Br_y: a global modeling study of $CHBr_3$ and CH_2Br_2, Atmos. Chem. Phys., 10, 2269–2286, doi:10.5194/acp-10-2269-2010, 2010.

Liang, Q., Atlas, E., Blake, D., Dorf, M., Pfeilsticker, K., and Schauffler, S.: Convective transport of very short lived bromocarbons to the stratosphere, Atmos. Chem. Phys., 14, 5781–5792, doi:10.5194/acp-14-5781-2014, 2014.

Lindberg, S. and Stratton, W.: Atmospheric mercury speciation: concentrations and behavior of reactive gaseous mercury in ambient air, Environ. Sci. Technol., 32, 49–57, doi:10.1021/es970546u, 1998.

Lin, J.-T. and McElroy, M. B.: Impacts of boundary layer mixing on pollutant vertical profiles in the lower troposphere: implications to satellite remote sensing, Atmos. Environ., 44, 1726–1739, doi:10.1016/j.atmosenv.2010.02.009, 2010.

Liu, G., Cai, Y., Kalla, P., Scheidt, D., Richards, J., Scinto, L. J., Gaiser, E., and Appleby, C.: Mercury mass budget estimates and cycling seasonality in the Florida everglades, Environ. Sci. Technol., 42, 1954–1960, doi:10.1021/es7022994, 2008.

Lyman, S. N. and Jaffe, D. A.: Formation and fate of oxidized mercury in the upper troposphere and lower stratosphere, Nat. Geosci., 5, 114–117, doi:10.1038/NGEO1353, 2012.

Lyman, S. N., Gustin, M. S., Prestbo, E. M., Kilner, P. I., Edgerton, E., and Hartsell, B.: Testing and application of surrogate surfaces for understanding potential gaseous oxidized mercury dry deposition, Environ. Sci. Technol., 43, 6235–6241, doi:10.1021/es901192e, 2009.

Marsh, D., Mills, M. J., Kinnison, D. E., Garcia, R. R., Lamarque, J.-F., and Calvo, N.: Climate change from 1850–2005 simulated in CESM1 (WACCM), J. Climate, 26, 7372–7391, doi:10.1175/JCLI-D-12-00558.1, 2013.

ACPD
15, 28317–28360, 2015

McGrath-Spangler, E. L. and Molod, A.: Comparison of GEOS-5 AGCM planetary boundary layer depths computed with various definitions, Atmos. Chem. Phys., 14, 6717–6727, doi:10.5194/acp-14-6717-2014, 2014.

Meller, R. and Moortgat, G.: Temperature dependence of the absorption cross sections of formaldehyde between 223 and 323 K in the wavelength range 225–375 nm, J. Geophys. Res.-Atmos., 105, 7089–7101, doi:10.1029/1999JD901074, 2000.

Nair, U. S., Wu, Y., Walters, J., Jansen, J., and Edgerton, E. S.: Diurnal and seasonal variation of mercury species at coastal-suburban, urban, and rural sites in the southeastern United States, Atmos. Environ., 47, 499–508, doi:10.1016/j.atmosenv.2011.09.056, 2012.

Nair, U. S., Wu, Y., Holmes, C. D., Ter Schure, A., Kallos, G., and Walters, J. T.: Cloud-resolving simulations of mercury scavenging and deposition in thunderstorms, Atmos. Chem. Phys., 13, 10143–10157, doi:10.5194/acp-13-10143-2013, 2013.

Parrella, J. P., Jacob, D. J., Liang, Q., Zhang, Y., Mickley, L. J., Miller, B., Evans, M. J., Yang, X., Pyle, J. A., Theys, N., and Van Roozendael, M.: Tropospheric bromine chemistry: implications for present and pre-industrial ozone and mercury, Atmos. Chem. Phys., 12, 6723–6740, doi:10.5194/acp-12-6723-2012, 2012.

Prados-Roman, C., Butz, A., Deutschmann, T., Dorf, M., Kritten, L., Minikin, A., Platt, U., Schlager, H., Sihler, H., Theys, N., Van Roozendael, M., Wagner, T., and Pfeilsticker, K.: Airborne DOAS limb measurements of tropospheric trace gas profiles: case studies on the profile retrieval of O_4 and BrO, Atmos. Meas. Tech., 4, 1241–1260, doi:10.5194/amt-4-1241-2011, 2011.

Pundt, I., Pommereau, J.-P., Chipperfield, M. P., van Roozendael, M., and Goutail, F.: Climatology of the stratospheric BrO vertical distribution by balloon-borne UV-visible spectrometry, J. Geophys. Res.-Atmos., 107, ACH 23-1–ACH 23-14, doi:10.1029/2002JD002230, 2002.

Read, K. A., Mahajan, A. S., Carpenter, L. J., Evans, M. J., Faria, B. V. E., Heard, D. E., Hopkins, J. R., Lee, J. D., Moller, S. J., Lewis, A. C., Mendes, L., McQuaid, J. B., Oetjen, H., Saiz-Lopez, A., Pilling, M. J., and Plane, J. M. C.: Extensive halogen-mediated ozone destruction over the tropical Atlantic Ocean, Nature, 453, 1232–1235, doi:10.1038/nature07035, 2008.

Rienecker, M. M., Suarez, M. J., Gelaro, R., Todling, R., Bacmeister, J., Liu, E., Bosilovich, M. G., Schubert, S. D., Takacs, L., Kim, G.-K., Bloom, S., Chen, J., Collins, D., Conaty, A., da Silva, A., Gu, W., Joiner, J., Koster, R. D., Lucchesi, R., Molod, A., Owens, T., Pawson, S., Pegion, P., Redder, C. R., Reichle, R., Robertson, F. R., Ruddick, A. G., Sienkiewicz, M., and Woollen, J.: MERRA: NASA's Modern-Era Retrospective Analysis for

ACPD
15, 28317–28360, 2015

Research and Applications, J. Climate, 24, 3624–3648, doi:10.1175/JCLI-D-11-00015.1, 2011.

Rodgers, C. D.: Inverse Methods for Atmospheric Sounding: Theory and Practice, World Scientific, Singapore, 2000.

Rothman, L. S., Jacquemart, D., Barbe, A., Benner, D. C., Birk, M., Brown, L. R., Carleer, M. R., Chackerian, C., Chance, K., Coudert, L. H., Dana, V., Devi, V. M., Flaud, J.-M., Gamache, R. R., Goldman, A., Hartmann, J.-M., Jucks, K. W., Maki, A. G., Mandin, J.-Y., Massie, S. T., Orphal, J., Perrin, A., Rinsland, C. P., Smith, M. A. H., Tennyson, J., Tolchenov, R. N., Toth, R. A., Vander Auwera, J., Varanasi, P., and Wagner, G.: The HITRAN 2004 molecular spectroscopic database, J. Quant. Spectrosc. Ra., 96, 139–204, doi:10.1016/j.jqsrt.2004.10.008, 2005.

Rutter, A. P. and Schauer, J. J.: The effect of temperature on the gas-particle partitioning of reactive mercury in atmospheric aerosols, Atmos. Environ., 41, 8647–8657, doi:10.1016/j.atmosenv.2007.07.024, 2007.

Saiz-Lopez, A., Lamarque, J.-F., Kinnison, D. E., Tilmes, S., Ordóñez, C., Orlando, J. J., Conley, A. J., Plane, J. M. C., Mahajan, A. S., Sousa Santos, G., Atlas, E. L., Blake, D. R., Sander, S. P., Schauffler, S., Thompson, A. M., and Brasseur, G.: Estimating the climate significance of halogen-driven ozone loss in the tropical marine troposphere, Atmos. Chem. Phys., 12, 3939–3949, doi:10.5194/acp-12-3939-2012, 2012.

Salawitch, R., Weisenstein, D., Kovalenko, L., Sioris, C., Wennberg, P., Chance, K., Ko, M., and McLinden, C.: Sensitivity of ozone to bromine in the lower stratosphere, Geophys. Res. Lett., 32, L05811, doi:10.1029/2004GL021504, 2005.

Sander, R., Keene, W. C., Pszenny, A. A. P., Arimoto, R., Ayers, G. P., Baboukas, E., Cainey, J. M., Crutzen, P. J., Duce, R. A., Hönninger, G., Huebert, B. J., Maenhaut, W., Mihalopoulos, N., Turekian, V. C., and Van Dingenen, R.: Inorganic bromine in the marine boundary layer: a critical review, Atmos. Chem. Phys., 3, 1301–1336, doi:10.5194/acp-3-1301-2003, 2003.

Schofield, R., Johnston, P. V., Thomas, A., Kreher, K., Connor, B. J., Wood, S., Shooter, D., Chipperfield, M. P., Richter, A., von Glasow, R., and Rodgers, C. D.: Tropospheric and stratospheric BrO columns over Arrival Heights, Antarctica, 2002, J. Geophys. Res-Atmos, 111, D22310, doi:10.1029/2005JD007022, 2006.

Schroeder, W. and Munthe, J.: Atmospheric mercury – an overview, Atmos. Environ., 32, 809–822, doi:10.1016/S1352-2310(97)00293-8, 1998.

ACPD
15, 28317–28360, 2015

Selin, N. E., Jacob, D. J., Yantosca, R. M., Strode, S., Jaeglé, L., and Sunderland, E. M.: Global 3-D land-ocean–atmosphere model for mercury: present-day versus preindustrial cycles and anthropogenic enrichment factors for deposition, Global Biogeochem. Cy., 22, GB2011, doi:10.1029/2007GB003040, 2008.

Selin, N. E., Sunderland, E. M., and Knightes, C. D.: Sources of mercury exposure for U. S. seafood consumers: implications for policy, Environ. Health Persp., 118, 137–143, doi:10.1289/ehp.0900811, 2010.

Sexauer Gustin, M., Weiss-Penzias, P. S., and Peterson, C.: Investigating sources of gaseous oxidized mercury in dry deposition at three sites across Florida, USA, Atmos. Chem. Phys., 12, 9201–9219, doi:10.5194/acp-12-9201-2012, 2012.

Shah, V., Jaeglé, L., Gratz, L. E., Ambrose, J. L., Jaffe, D. A., Selin, N. E., Song, S., Campos, T. L., Flocke, F. M., Reeves, M., Stechman, D., Stell, M., Festa, J., Stutz, J., Weinheimer, A. J., Knapp, D. J., Montzka, D. D., Tyndall, G. S., Apel, E. C., Hornbrook, R. S., Hills, A. J., Riemer, D. D., Blake, N. J., Cantrell, C. A., and Mauldin III, R. L.: Origin of oxidized mercury in the summertime free troposphere over the southeastern US, Atmos. Chem. Phys. Discuss., 15, 26839–26893, doi:10.5194/acpd-15-26839-2015, 2015.

Shepler, B., Balabanov, N., and Peterson, K.: Ab initio thermochemistry involving heavy atoms: an investigation of the reactions Hg + IX (X = 1, Br, Cl, O), J. Phys. Chem. A, 109, 10363–10372, doi:10.1021/jp0541617, 2005.

Sihler, H., Platt, U., Beirle, S., Marbach, T., Kühl, S., Dörner, S., Verschaeve, J., Frieß, U., Pöhler, D., Vogel, L., Sander, R., and Wagner, T.: Tropospheric BrO column densities in the Arctic derived from satellite: retrieval and comparison to ground-based measurements, Atmos. Meas. Tech., 5, 2779–2807, doi:10.5194/amt-5-2779-2012, 2012.

Soerensen, A. L., Sunderland, E. M., Holmes, C. D., Jacob, D. J., Yantosca, R. M., Skov, H., Christensen, J. H., Strode, S. A., and Mason, R. P.: An improved global model for air–sea exchange of mercury: high concentrations over the North Atlantic, Environ. Sci. Technol., 44, 8574–8580, doi:10.1021/es102032g, 2010.

Spietz, P., Martin, J. C. G., and Burrows, J.P: Spectroscopic studies of the I_2/O_3 photochemistry – Part 2. Improved spectra of iodine oxides and analysis of the IO absorption spectrum, J. Photoch. Photobio. A, 50, 1–3, doi:10.1016/j.jphotochem.2005.08.023, 2005.

Streets, D., Zhang, Q., and Wu, Y.: Projections of global mercury emissions in 2050, Environ. Sci. Technol., 43, 2983–2988, doi:10.1021/es802474j, 2009.

ACPD
15, 28317–28360, 2015

Swartzendruber, P. C., Jaffe, D. A., Prestbo, E. M., Weiss-Penzias, P., Selin, N. E., Park, R., Jacob, D. J., Strode, S., and Jaeglé, L.: Observations of reactive gaseous mercury in the free troposphere at the Mount Bachelor Observatory, J. Geophys. Res., 111, D24301, doi:10.1029/2006JD007415, 2006.

Swartzendruber, P. C., Jaffe, D. A., and Finley, B.: Development and first results of an aircraft-based, high time resolution technique for gaseous elemental and reactive (oxidized) gaseous mercury, Environ. Sci. Technol., 43, 7484–7489, 2009.

Thalman, R. and Volkamer, R.: Temperature dependent absorption cross-sections of O_2-O_2 collision pairs between 340 and 630 nm and at atmospherically relevant pressure, Phys. Chem. Chem. Phys., 15, 15371–15381, doi:10.1039/c3cp50968k, 2013.

Theys, N., Van Roozendael, M., Hendrick, F., Fayt, C., Hermans, C., Baray, J.-L., Goutail, F., Pommereau, J.-P., and De Mazière, M.: Retrieval of stratospheric and tropospheric BrO columns from multi-axis DOAS measurements at Reunion Island (21° S, 56° E), Atmos. Chem. Phys., 7, 4733–4749, doi:10.5194/acp-7-4733-2007, 2007.

Theys, N., Van Roozendael, M., Hendrick, F., Yang, X., De Smedt, I., Richter, A., Begoin, M., Errera, Q., Johnston, P. V., Kreher, K., and De Mazière, M.: Global observations of tropospheric BrO columns using GOME-2 satellite data, Atmos. Chem. Phys., 11, 1791–1811, doi:10.5194/acp-11-1791-2011, 2011.

Tossell, J. A.: Calculation of the energetics for oxidation of gas-phase elemental Hg by Br and BrO, J. Phys. Chem. A, 107, 7804–7808, doi:10.1021/jp030390m, 2003.

Vandaele, A. C., Hermans, C., Simon, P. C., Carleer, M., Colin, R., Fally, S., Mérienne, M. F., Jenouvrier, A., and Coquart, B.: Measurements of the NO_2 absorption cross-section from 42 000 cm^{-1} to 10 000 cm^{-1} (238–1000 nm) at 220 K and 294 K, J. Quant. Spectrosc. Ra., 59, 171–184, doi:10.1016/S0022-4073(97)00168-4, 1998.

Van Roozendael, M., Wagner, T., Richter, A., Pundt, I., Arlander, D., Burrows, J., Chipperfield, M., Fayt, C., Johnston, P., Lambert, J., Kreher, K., Pfeilsticker, K., Platt, U., Pommereau, J., Sinnhuber, B., Tornkvist, K., and Wittrock, F.: Intercomparison of BrO measurements from ERS-2 GOME, ground-based and balloon platforms, Adv. Space Res., 29, 1661–1666, doi:10.1016/S0273-1177(02)00098-4, 2002.

Volkamer, R., Spietz, P., Burrows, J., and Platt, U.: High-resolution absorption cross-section of glyoxal in the UV-vis and IR spectral ranges, J. Photoch. Photobio. A., 172, 35–46, doi:10.1016/j.jphotochem.2004.11.011, 2005.

ACPD
15, 28317–28360, 2015

Volkamer, R., Baidar, S., Campos, T. L., Coburn, S., DiGangi, J. P., Dix, B., Eloranta, E. W., Koenig, T. K., Morley, B., Ortega, I., Pierce, B. R., Reeves, M., Sinreich, R., Wang, S., Zondlo, M. A., and Romashkin, P. A.: Aircraft measurements of BrO, IO, glyoxal, NO_2, H_2O, O_2–O_2 and aerosol extinction profiles in the tropics: comparison with aircraft-/ship-based in situ and lidar measurements, Atmos. Meas. Tech., 8, 2121–2148, doi:10.5194/amt-8-2121-2015, 2015.

Wang, S., Schmidt, J. A., Baidar, S., Coburn, S., Dix, B., Koenig, T., Apel, E. C., Bowdalo, D., Campos, T. L., Eloranta, E., Evans, M. J., diGangi, J. P., Zondlo, M. A., Gao, R. S., Haggerty, J. A., Hall, S. R., Hornbrook, R. S., Jacob, D. J., Morley, B., Pierce, B. R., Reeves, M., Romashkin, P. A., ter Schure, A., and Volkamer, R.: Active and widespread halogen chemistry in the tropical and subtropical free troposphere, P. Natl. Acad. Sci. USA, 112, 9281–9286, doi:10.1073/pnas.1505142112, 2015.

Weiss-Penzias, P. S., Gustin, M. S., and Lyman, S. N.: Source of gaseous oxidized mercury and mercury dry deposition at two southeastern U. S. sites, Atmos. Environ., 45, 4569–4579, doi:10.1016/j.atmosenv.2011.05.069, 2011.

Weiss-Penzias, P., Amos, H. M., Selin, N. E., Gustin, M. S., Jaffe, D. A., Obrist, D., Sheu, G.-R., and Giang, A.: Use of a global model to understand speciated atmospheric mercury observations at five high-elevation sites, Atmos. Chem. Phys., 15, 1161–1173, doi:10.5194/acp-15-1161-2015, 2015.

Wilmouth, D., Hanisco, T., Donahue, N., and Anderson, J.: Fourier transform ultraviolet spectroscopy of the A2Π3/2<-X2Π3/2 transition of BrO, J. Phys. Chem. A, 103, 8935–8945, doi:10.1021/jp991651o, 1999.

Yang, X., Cox, R. A., Warwick, N. J., Pyle, J. A., Carver, G. D., O'Connor, F. M., and Savage, N. H.: Tropospheric bromine chemistry and its impacts on ozone: a model study, J. Geophys. Res.-Atmos., 110, D23311, doi:10.1029/2005JD006244, 2005.

Zhang, Y., Jaeglé, L., van Donkelaar, A., Martin, R. V., Holmes, C. D., Amos, H. M., Wang, Q., Talbot, R., Artz, R., Brooks, S., Luke, W., Holsen, T. M., Felton, D., Miller, E. K., Perry, K. D., Schmeltz, D., Steffen, A., Tordon, R., Weiss-Penzias, P., and Zsolway, R.: Nested-grid simulation of mercury over North America, Atmos. Chem. Phys., 12, 6095–6111, doi:10.5194/acp-12-6095-2012, 2012.

ACPD
15, 28317–28360, 2015

Table 1. Overview of DOAS settings.

Cross Section, Parameter	Reference	BrO window (338–359 nm)	IO window (415–438 nm)	NO_2 window (434–460 nm)	O_4 window (437–486 nm)
Polynomial Order		5	5	3	5
O_3 T = 223 K	Bogumil et al. (2003)	X	X	X	X
O_3 T = 243 K	Bogumil et al. (2003)	X	X	X	X
NO_2 T = 220 K	Vandaele et al. (1997)	X	X	X	X
NO_2 T = 220 K	Vandaele et al. (1997)	X	X	X	X
O_4 T = 293	Thalman and Volkamer (2013)	X		X	X
BrO	Wilmouth et al. (1999)	X			
HCHO	Meller and Moortgat (2000)	X			
IO	Spietz et al. (2005)		X		
CHOCHO	Volkamer et al. (2005)			X	
H_2O	Rothman et al. (2005)			X	X

ACPD
15, 28317–28360, 2015

Table 2. Summary of mercury reactions and rate coefficients used in box-model.

Reaction	Rate or equilibrium[1] Coefficient[2]	Reference
$Hg^0 + O_3 \rightarrow HgO + O_2$	3×10^{-20}	Hall (1995)
$HgO_{(g)} \leftrightarrow HgO_{(aq)}$	K_{eq}[1]	Rutter and Schauer (2007)
$HgO_{(aq)} \rightarrow Hg^0_{(g)}$	1.12×10^{-5}	Costa and Liss (1999)
$Hg^0 + Cl \xrightarrow{M,Br} HgClBr$[3]	$2.2 \times 10^{-32} \times \exp\left(680 \times \left(\frac{1}{T} - \frac{1}{298}\right)\right) \times [M]$	Donohoue (2005)
$HgClY_{(g)} \leftrightarrow HgClY_{(aq)}$	K_{eq}[1]	Rutter and Schauer (2007)
$HgClY_{(aq)} \rightarrow Hg^0_{(g)}$	1.12×10^{-5}	Costa and Liss (1999)
$Hg^0 + Br \xrightarrow{M} HgBr$	$1.46 \times 10^{-32} \times \left(\frac{T}{298}\right)^{-1.86} \times [M]$	Donohoue (2006)
$HgBr + M \rightarrow Hg^0 + Br + M$	$4.0 \times 10^{9} \times \exp\left(\frac{-7292}{T}\right)$	Goodsite et al. (2012)
$HgBr_{(g)} \leftrightarrow HgBr_{(aq)}$	K_{eq}[1]	Rutter and Schauer (2007)
$HgBr + Y$[4] $\rightarrow HgBrY$	$2.5 \times 10^{-10} \times \left(\frac{T}{298}\right)^{-0.57}$	Goodsite et al. (2004)
$\rightarrow Hg^0 + Br_2$	3.9×10^{-11}	Balabanov et al. (2005)
$HgBrY_{(g)} \leftrightarrow HgBrY_{(aq)}$	K_{eq}[1]	Rutter and Schauer (2007)
$HgBrY_{(aq)} \rightarrow Hg^0_{(g)}$	1.12×10^{-5}	Costa and Liss (1999)
$HgBr + Y'$[5] $\rightarrow HgBrY'$	1×10^{-10}	Dibble et al. (2012)
$HgBrY'_{(g)} \leftrightarrow HgBrY'_{(aq)}$	K_{eq}[1]	Rutter and Schauer (2007)
$HgBrY'_{(aq)} \rightarrow Hg^0_{(g)}$	1.12×10^{-5}	Costa and Liss (1999)

[1] Equilibrium coefficient is parameterized according to Rutter and Schauer (2007): $K_{eq} = (SA - PM)/10^{((-4250/T)+10)}$, where SA = the specific aerosol surface area, and PM = the particulate mass.
[2] Rate coefficients are given in either $cm^3\,molec^{-1}\,s^{-1}$ or s^{-1}.
[3] Assumes that the reaction between Hg^0 and Cl is the rate limiting step to form HgCl which will then quickly react with Br to form HgClBr.
[4] Y = Br, OH.
[5] Y' = HO_2, NO_2, BrO, IO, I.

ACPD
15, 28317–28360, 2015

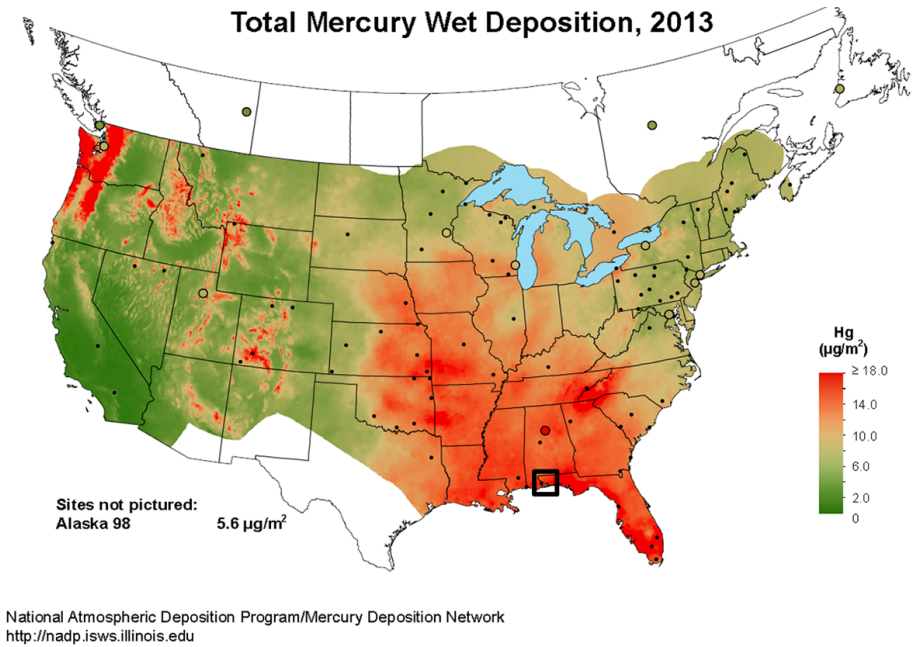

Figure 1. Total mercury wet deposition in the US for 2013. The highest levels of Hg deposition are observed in the southeastern US, where no local and regional sources are located immediately upwind. The black square indicates the measurement location.

ACPD
15, 28317–28360, 2015

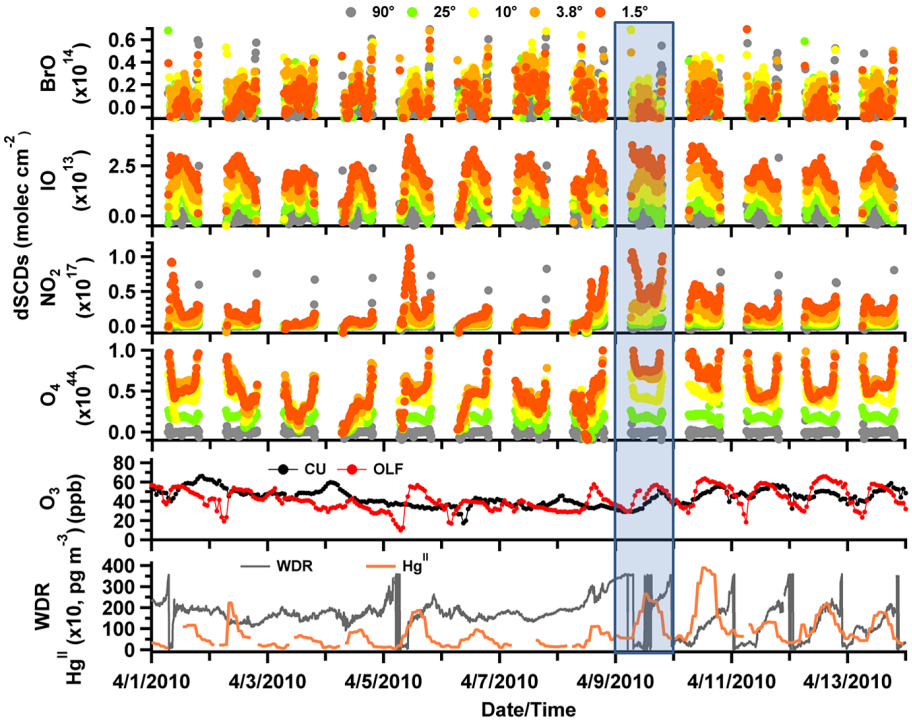

Figure 2. Overview of the MAX-DOAS measurements for the week surrounding the case study day (9 April, highlighted with blue box). Also included are O_3 measurements from a monitor collocated with the MAX-DOAS instrument (label "CU", black trace) and a monitor located at an Mercury Deposition Network (MDN) site ~ 30 km northwest of the EPA site (label "OLF", red trace), and wind direction measurements (grey trace) from a site near the EPA facility along with HgII measurements from the MDN site (scaled by a factor of 10, orange trace).

ACPD
15, 28317–28360, 2015

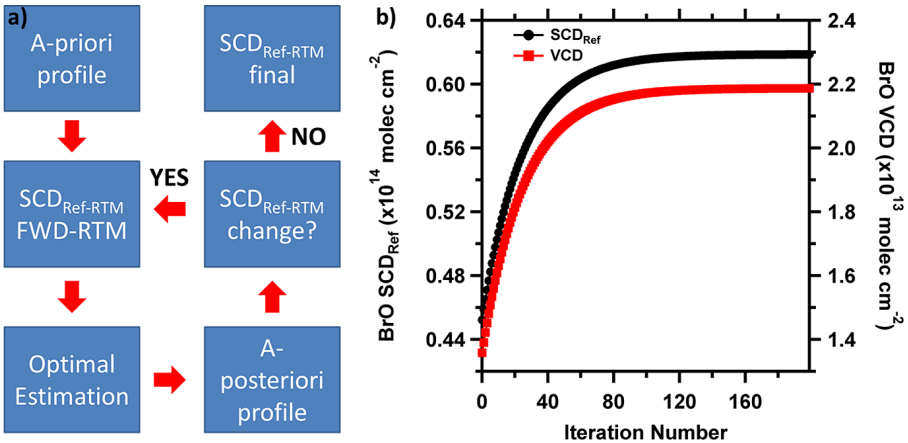

Figure 3. Conceptual sketch of the SCD_{Ref} retrieval **(a)**, and resulting SCD_{Ref} values (black trace). The sensitivity of the a-posteriori BrO VCD (red trace) to SCD_{Ref} is also shown **(b)**.

ACPD
15, 28317–28360, 2015

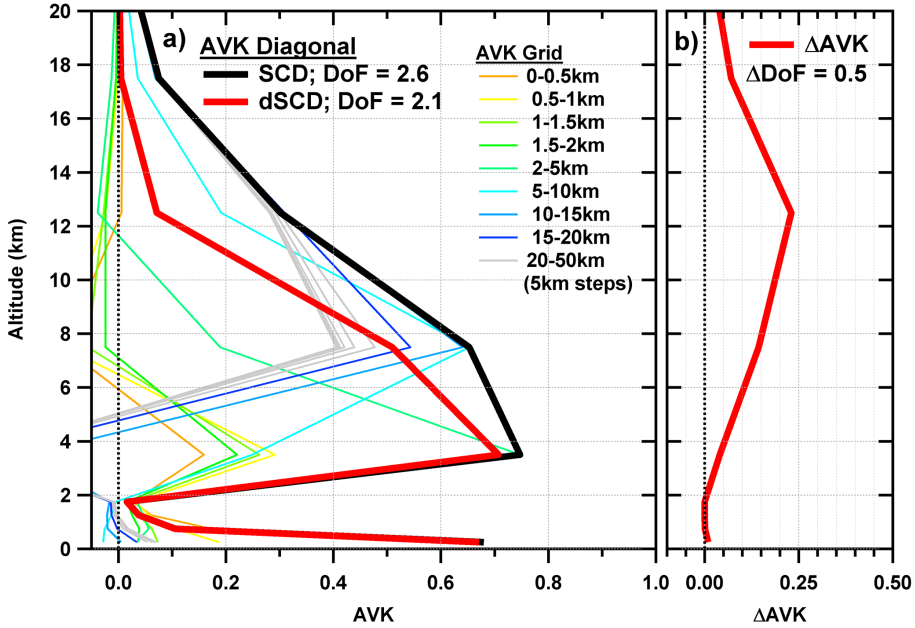

Figure 4. Characterizing the retrieval averaging kernel (AVK) and Degrees of Freedom (DoF). **(a)** AVK output for an inversion of BrO SCDs (at SZA = 25°) as a function of altitude. The colored traces represent the individual altitude grids of the inversion accounting for SCD_{Ref}; the thick black trace is the diagonal of the AVK matrix; the thick red trace is the diagonal of the AVK matrix from the inversion not accounting for SCD_{Ref}. **(b)** shows the difference between the two AVK diagonals as a function of altitude.

ACPD
15, 28317–28360, 2015

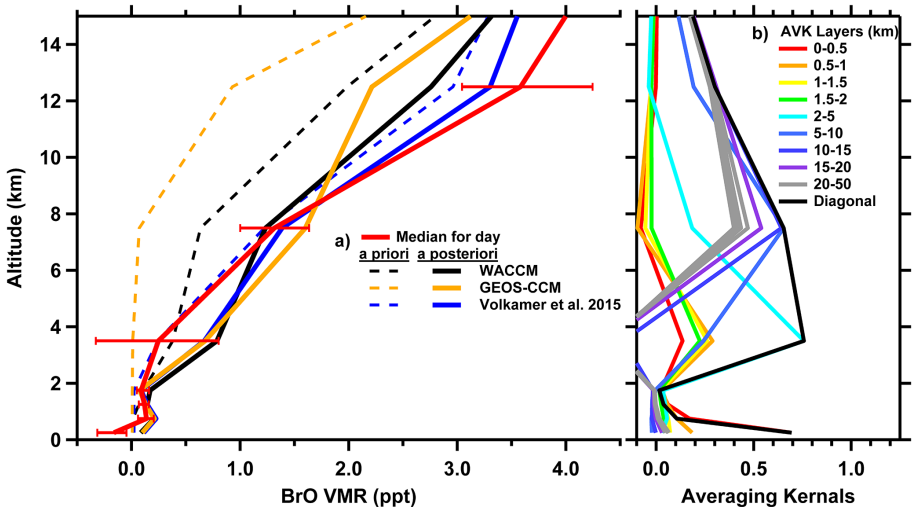

Figure 5. BrO profiles for a single MAX-DOAS measurement scan at SZA ∼ 23° around solar noon. **(a)** contains three of the a-priori profiles tested (dashed lines) and the respective a-posteriori profiles (solid lines); colors correspond to use of WACCM (black); GEOS-CCM (orange); and TORERO RF12 (blue) as a-priori information. **(b)** contains the AVK from the inversion using the WACCM profile as the a-priori, and gives an indication on the amount of information coming from the measurements as a function of altitude.

ACPD
15, 28317–28360, 2015

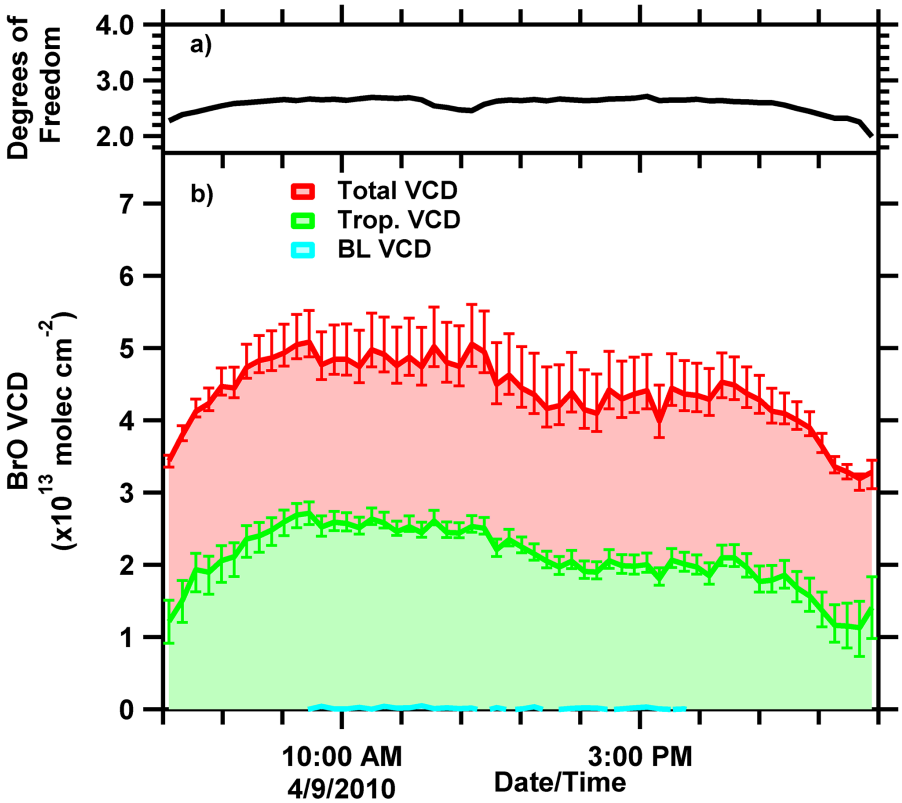

Figure 6. Graphic of the diurnal variation in the BrO vertical profiles represented as partial VCDs for the BL (0–1 km), troposphere (0–15 km), total (0–50 km) **(b)**, and the total DoFs from the inversion for each profile in **(a)**. The error bars on the VCDs indicate the range of values retrieved using the three different a-priori profiles.

ACPD
15, 28317–28360, 2015

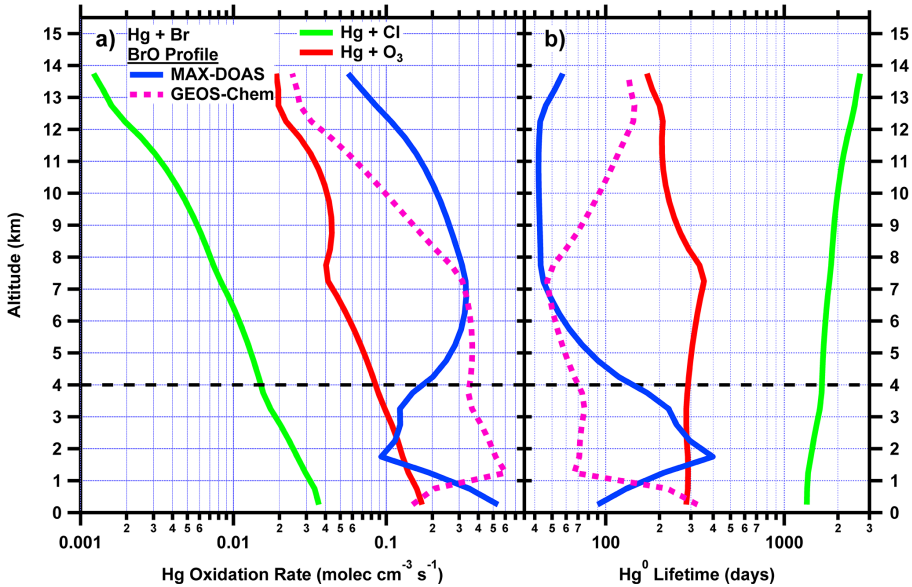

Figure 7. Box model results of the rate of mercury oxidation as a function of altitude for three species: (1) chlorine radicals (green), (2) ozone (red), and (3) bromine radicals (solid blue: MAX-DOAS; dashed pink: GEOS-Chem) **(a)**; the corresponding lifetimes are found in **(b)**. The black dashed line at 4 km shows where measurement sensitivity starts to drop because of the decreasing amount of BrO (the measured parameter) in the lower layers of the atmosphere.

ACPD
15, 28317–28360, 2015

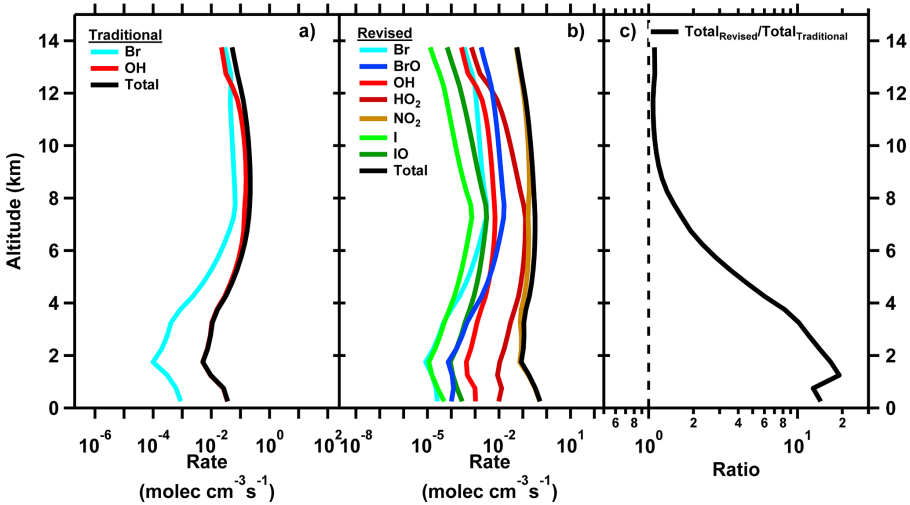

Figure 8. Box model results for the scavenging of the HgBr adduct as a function altitude for two different reaction schemes: traditional **(a)** and revised **(b)**. **(c)** contains the ratio of the total rates (black traces in panels **a** and **b**) to show the enhancement in the rate of the scavenging reaction when other reactants are taken into consideration.

ACPD
15, 28317–28360, 2015

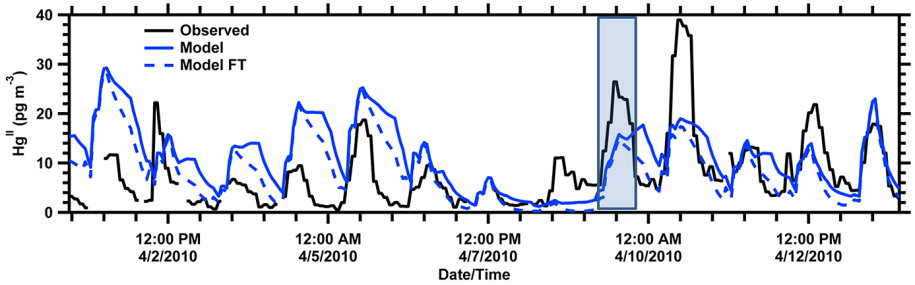

Figure 9. Observed (black solid trace) and simulated (blue traces) concentrations of oxidized mercury (Hg^{II} = GOM + PBM) during April 2010 (9 April highlighted). Model results from GEOS-Chem (solid) include a sensitivity test, labeled FT (dashed trace), in which North American anthropogenic emissions are zero and no GEM oxidation occurs in the lower troposphere (> 700 hPa); therefore all Hg^{II} in the "FT" model is derived from oxidation of in the free troposphere or long-range transport.

ACPD
15, 28317–28360, 2015